NAG 5-8397

Probing the Physics of Active Galactic Nuclei by Multiwavelength Monitoring
ASP Conference Series, Vol. 224, 2001
B.M. Peterson, R.S. Polidan, and R.W. Pogge

Observational Definition of Future AGN Echo-Mapping Experiments

Stefan Collier and Bradley M. Peterson

Department of Astronomy, The Ohio State University, Columbus, OH 43210

Keith Horne

School of Physics and Astronomy, University of St. Andrews, North Haugh, St. Andrews, Fife, KY16 9SS, United Kingdom

Abstract. We describe numerical simulations we have begun in order to determine the observational requirements for future echo-mapping experiments. We focus on two particular problems: (1) determination of the structure and kinematics of the broad-line region through emission-line reverberation mapping, and (2) detection of interband continuum lags that may be used as a probe of the continuum source, presumably a temperature-stratified accretion disk. Our preliminary results suggest the broad-line region can be reverberation-mapped to good precision with spectra of signal-to-noise ratio per pixel $S/N \approx 30$, time resolution $\Delta t \approx 0.1$ day, and duration of about 60 days (which is a factor of three larger than the longest time scale in the input models); data that meet these requirements do not yet exist. We also find that interband continuum lags of $\gtrsim 0.5$ days can be detected at $\gtrsim 95\%$ confidence with at least daily observations for about 6 weeks, or rather more easily and definitively with shorter programs undertaken with satellite-based observatories. The results of these simulations show that significant steps forward in multiwavelength monitoring will almost certainly require dedicated facilities.

1. Introduction

Nearly thirty years ago, Bahcall, Kozlovsky, & Salpeter (1972) proposed that broad emission-line variability in active galactic nuclei (AGNs) could be used to determine the structure and kinematics of the broad-line region (BLR). The clear detection of correlated continuum/emission-line variations several years later rekindled interest in this concept (Fabrika 1980; Blandford & McKee 1982; Capriotti, Foltz, & Peterson 1982). Blandford & McKee (1982) developed the mathematical formalism of what has become known as "reverberation mapping" or "echo mapping," a technique of mapping the phase-space distribution of BLR emission through analysis of the detailed emission-line response to continuum variations. In the simple linear theory, the broad emission-line line-of-sight (Doppler) velocity and time-dependent response $L(V_z, t)$ is a convolution of prior, time-delayed continuum variations $C(t-\tau)$ with a "transfer function" $\Psi(V_z,\tau)$ such that

$$L(V_z,t) = \int_{-\infty}^{\infty} \Psi(V_z,\tau)C(t-\tau)\,d\tau. \tag{1}$$

The transfer function $\Psi(V_z,\tau)$ is a projection of the six-dimenisional (three spatial and three kinematic) phase-space distribution into two dimensions (V_z and τ). This is a tremendous improvement over the highly ambiguous information available from the line profile alone, and strongly constrains the geometry and kinematics of the BLR. The results may be further strengthened by concomitant photoionization equilibrium modeling (see Horne, these proceedings) and/or simple symmetry considerations. The operational goal of reverberation studies is to use the observables, the velocity-resolved emission-line light curve $L(V_z,t)$ and the continuum light curve $C(t)$, to recover $\Psi(V_z,\tau)$ uniquely. An equivalent formalism may be applied to the relationship between continuum variations at different wavelengths to recover a two-dimensional transfer function $\Psi(\lambda,\tau)$ which does not include kinematic information.

Successful application of echo-mapping techniques to AGN variability data have led to a number of important conclusions. These include:

1. The BLR is small, $\sim 10^{-3}$–10^{-2} parsecs, and has a radially stratified ionization structure (e.g., Clavel et al. 1991; Peterson et al. 1991).

2. The anticorrelation of emission-line time delays and line widths provides excellent evidence for centrally located supermassive black holes of mass $M \approx 10^6$–$10^8\,M_\odot$ (Peterson & Wandel 2000; see also Peterson, these proceedings).

3. The partially resolved line-of-sight velocity-dependent broad-line response indicates that the BLR kinematics are probably not dominated by radial motions (Wanders et al. 1995; Done & Krolik 1996; Ulrich & Horne 1996).

4. The close coupling of continuum variations at, e.g, UV and optical wavelengths suggests that the various continuum emitting regions must be radiatively coupled (e.g., Edelson et al. 1996).

More complete discussions on echo-mapping methodology and its results may be found in a number of review articles, including those of Horne (1999), Netzer & Peterson (1997), and Peterson (1993).

Currently, only non-degenerate solutions to $\Psi(V_z,\tau)$ exist for NGC 4151 (Ulrich & Horne 1996) and NGC 5548 (Wanders et al. 1995; Done & Krolik 1996). These demonstrate the gross kinematic structure of the C IV λ1549 emission region is not dominated by radial gas motions, as the blueshifted and redshifted parts of the emission line respond indistinguishably. However, there was earlier evidence to the contrary (Crenshaw & Blackwell 1991). A possible infalling kinematic component may be suggested by some of the data, but the results remain ambigious. The data are grossly consistent with, at least, hydromagnetic disk-wind models and those incorporating spherical distributions of clouds in Keplerian orbits. A unique solution, one breaking the consistency of the data with multiple BLR models, remains elusive because current data sets do not have the required combination of signal-to-noise ratio S/N, monitoring duration, and temporal resolution, and are typically deficient in more than one of these attributes.

While clear progress has been made in the study of emission-line variability, the detailed relationship between multicolor continuum variations remains unclear on account of observational ambiguities and/or complexities arising from possible different continuum emission components (e.g., disk and diffuse-continuum emission; see Nandra and Korista & Goad, these proceedings). For one source, NGC 7469, optical variations were found to lag those at UV wavelengths by about 1–2 days (Wanders et al. 1997; Collier et al. 1998; Kriss et al. 2000). The emission strength and the magnitude and wavelength-dependence of the lags is approximately consistent with the standard black-hole–accretion-disk paradigm (Collier et al. 1999; Berkley et al. 2000, see §4). On the other hand, the 2–10 keV X-ray variations are not obviously correlated with the UV/optical continuum fluxes (Nandra et al. 1998), although there are indications from the spectral slope that the unobserved *soft* X-rays are correlated with the UV/optical variations (Nandra et al. 2000). This suggests a model that mixes both Comptonization and reprocessing, UV radiation from the disk is Compton upscattered by electrons in a hot corona into EUV/soft X-ray radiation, which radiatively drives variations at longer UV/optical wavelengths. This type of scenario may or may not be applicable to other sources, such as NGC 5548, in which the X-ray/EUV/UV variations are all closely coupled (Clavel et al. 1992; Marshall et al. 1997; Chiang et al. 2000). Furthermore, for NGC 3516 uncorrelated X-ray and optical variability was observed, and expected optical delays of ~ 0.1 days were not detected (Edelson et al. 2000).

It is clear that future progress in both mapping the BLR phase-space distribution and constraining the continuum source origin will require carefully designed simultaneous multiwavelength observations. This paper presents preliminary numerical simulations that were undertaken to define requirements for future AGN monitoring programs. In particular, our goals are:

1. To define the observational requirements of future monitoring campaigns that will allow us to distinguish among currently viable BLR models. The main variables are S/N of the data, the time interval between observations, and program duration.

2. To quantify the observability of expected time delays between multicolor continuum variations, thereby strongly constrain the continuum source structure and possibly measure its temperature profile.

We discuss the emission-line and continuum variability simulations separately. In §2, we outline our emission-line simulation methodology and describe briefly the specific models that we will try to distinguish among observationally. Our preliminary results are presented in §3. In §4, we discuss our simulation methodology pertaining to interband continuum relationships, and our preliminary results are presented in §5. We conclude with an overview of our simulation results in §6.

2. Emission-Line Simulation Methodology

Our simulation methodology is underpinned by assessing the observational characteristics, i.e., S/N, monitoring duration, and temporal resolution, required to distinguish among plausible BLR models.

The models we have chosen to compare to simulated data are based on the C IV λ1549 line in NGC 5548; derived either directly or rather loosely from the 39-day program of daily monitoring with the *HST* Faint Object Spectrograph in 1993 (Korista et al. 1995). They define several BLR models that are not distinguishable from one another with existing high-quality data. The requirement that we *must* be able to distinguish among them imposes a standard that is clearly a significant leap forward from what has been accomplished to date. To make the simulations both reasonable and relevant, we choose observational parameters appropriate for the baseline model of the *Kronos* multiwavelength observatory (Polidan & Peterson, these proceedings), which will be submitted to NASA for consideration as a Medium Explorer (MIDEX). These simulations are conservative in the sense that we are assuming the original design parameters for *Kronos*, as outlined in these proceedings by Polidan & Peterson; *Kronos* has recently undergone a re-design that will give UV/optical throughput nearly an order of magnitude greater than in the original design.

We first generate artificial continuum light curves $C(t)$ that mimic the behavior of the UV/optical continua of nearby, bright Seyfert 1 galaxies, as described in §2.1. These light curves are convolved with four model transfer functions $\Psi_{\rm mod}(V_z, \tau)$, as described in §2.2, according to eq. (1). This results in synthetic emission-line variations $L(V_z, t)$. We simulate the effects of random noise by altering the "observations" by random Gaussian deviates of appropriate amplitude. We use the simulated observations, $C(t)$ and $L(V_z, t)$, to recover an "observed" transfer function $\Psi_{\rm obs}(V_z, \tau)$, which we then compare with the original input model function $\Psi_{\rm mod}(V_z, \tau)$. We repeat these simulations a number of times in an effort to find the minimum monitoring characteristics that lead to a robust determination of the transfer function. We describe the above simulation procedure in more detail below.

2.1. Generating Artifical Light Curves $L(V_z, t)$ and $C(t)$

Power-spectrum analysis may be used to measure the variability power distribution as a function of temporal frequency (or equivalently time), and affords a method of characterizing AGN continuum variations. The power-density spectra (PDS) of AGNs may be parameterized as a power law $P(f) \propto f^{-\alpha}$, though the actual form is comparatively ill-defined. A PDS index $\alpha \approx 1.5$, was first estimated from long-look hard X-ray observations with *EXOSAT* (Lawrence & Papadakis 1993; Green, McHardy, & Lehto 1993). At lower photon energies, the PDS is even more poorly constrained, so we elected to use $\alpha = 1.5$. This results in continuum light curves that are similar to observed AGN light curves; moreover, the choice of a flatter rather than steeper PDS necessitates more complete sampling of the light curve, which makes this a conservative choice for our purposes.

We generate artifical continuum light curves $C(t)$ from a given power-density spectrum by Fourier transforming the PDS, with random phases for each frequency. In more recent simulations, as described in §4, α is drawn at random from a Gaussian distribution with mean μ and standard deviation σ chosen to match approximately the observed range, i.e., $\mu = 1.5$ and $\sigma = 0.5$.

The synthetic light curves $C(t)$ are normalized to have nominal fractional flux variations $F_{\rm var} = 0.16$ on time scales of one month; $F_{\rm var}$ is the amplitude of intrinsic variability relative to the mean flux, and is sometimes also known as the normalized variability amplitude. This level of fractional flux variability matches the observed UV $F_{\rm var}$ for bright, nearby Seyfert 1 AGN, as seen in Fig. 1. For each realization, the normalized continuum light curve $C(t)$ is convolved with the theoretical transfer function $\Psi_{\rm mod}(V_z, \tau)$ (§2.2), resulting in synthetic emission-line variations $L(V_z, t)$. The data set defined by $C(t)$ and $L(V_z, t)$, sampled like real observations and, with appropriate Gaussian-distributed noise added, are then analyzed as though they were real data, using the techniques of §2.3 to recover the "observed" transfer function $\Psi_{\rm obs}(V_z, \tau)$. We may then compare $\Psi_{\rm mod}(V_z, \tau)$ and $\Psi_{\rm obs}(V_z, \tau)$ to determine how well the transfer function is recovered, as described in §3.

2.2. Transfer Functions for Theoretical BLR Models $\Psi_{\rm mod}(V_z, \tau)$

The construction and appearance of model transfer functions $\Psi_{\rm mod}(V_z, \tau)$ for a variety of BLR models is discussed widely in the literature (e.g., Welsh & Horne 1991; Pérez et al. 1992).

We consider four plausible BLR models:

1. Model A is a spherical distribution of clouds in circular Keplerian orbits, illuminated by an anisotropic continuum source (e.g., Goad & Wanders 1996).
2. Model B is a flat rotating disk distribution of emitting clouds.
3. Model C is a hydromagnetic wind model, as described by Emmering, Blandford & Shlosman (1992).
4. Model D is a spherical distribution of clouds in Keplerian orbits.

Figure 2 shows as greyscale images the model transfer functions $\Psi_{\rm mod}(V_z, \tau)$ for these models. For each model, the smaller upper-right and lower-left panels represent the one dimensional transfer function $\Psi(\tau) = \int \Psi(V_z, \tau)\, dV_z$ and the emission-line profile $\Psi(V_z) = \int \Psi(V_z, \tau)\, d\tau$, respectively. Note $\Psi(\tau)$ for these models are similar and would in fact be indistinguishable at low resolution. The line profiles alone cannot be used to discriminate among individual models because of blending with non-variable components. In each of these models, the emission-line response extends only to time lags $\tau \lesssim 20$ days.

2.3. Recovering the Observed Transfer Functions $\Psi_{\rm obs}(V_z, \tau)$

Determination of $\Psi_{\rm obs}(V_z, \tau)$ from the data $C(t)$ and $L(V_z, t)$ represents a classical inversion problem in theoretical physics. The obvious method of solution is Fourier deconvolution, as originally suggested by Blandford & McKee (1982). In practice, use of Fourier methods is complicated by the data quality (i.e., the limited S/N of the data), quantity (the data trains are finite in length), and the

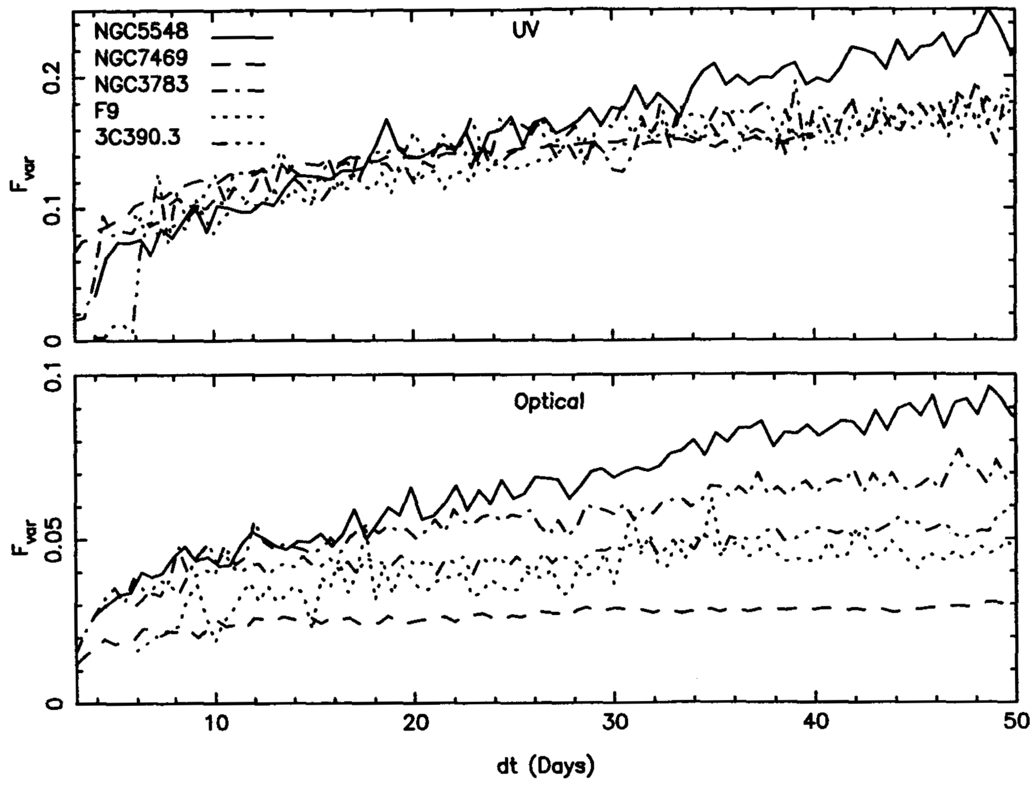

Figure 1. The amplitude of intrinsic variability relative to mean flux, F_{var}, as a function of time difference between pairs of data points for UV (top panel) and optical (bottom panel) spectroscopic observations of five Seyfert 1 galaxies. Typical UV/optical aperiodic fractional flux variations of ~ 16% in the UV and ~ 5% on time scales of one month are observed. The lower observed optical variability amplitude is largely due to host-galaxy contamination.

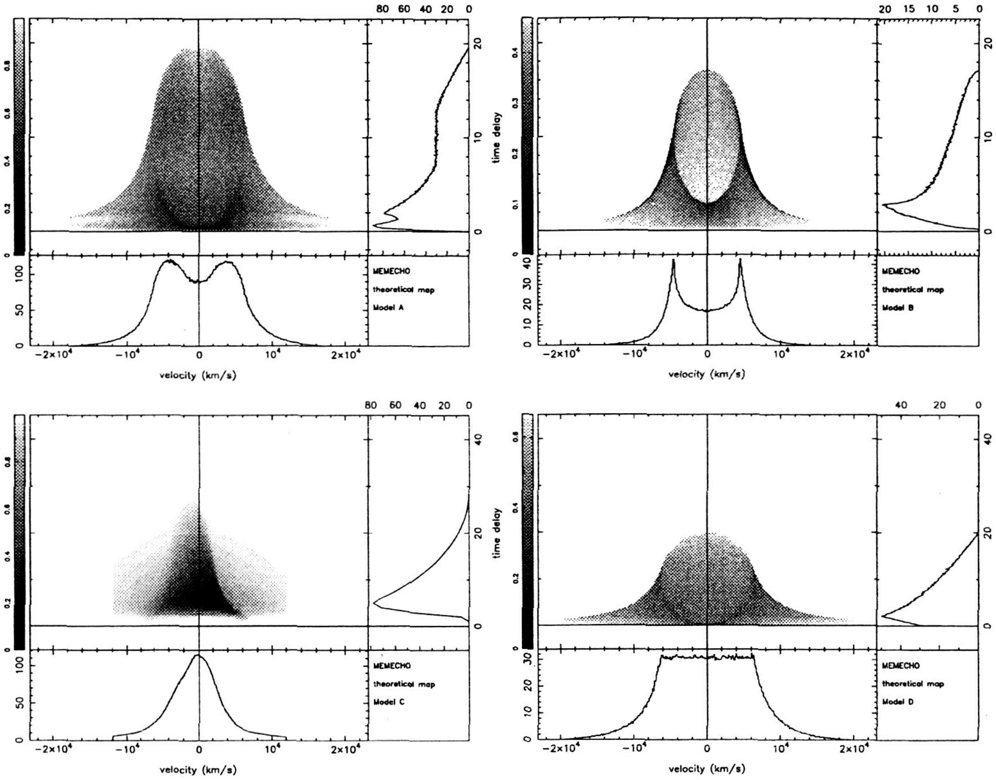

Figure 2. Representative model transfer functions are shown for the four models considered here, as labelled and discussed in §2.2: they are Model A (upper left), Model B (upper right), Model C (lower left), and Model D (lower right). For each model, three panels are shown: the large panel in the upper left is a grayscale rendering of the transfer function $\Psi_{\rm mod}(V_z, \tau)$. The upper right panel shows the one-dimensional transfer function $\Psi_{\rm mod}(\tau)$, i.e., $\Psi_{\rm mod}(V_z, \tau)$ integrated over line-of-sight velocity, and gives the total line flux as a function of τ. The lower left panel shows $\Psi_{\rm mod}(V_z, \tau)$ integrated over time, and represents the variable component of the emission-line profile. Note the similarity of $\Psi_{\rm mod}(\tau)$ for these models. The line profiles alone may not be used to discriminate among these models because of blending with non-variable components.

irregular sampling inherent in astronomical observations. These complications motivated development of a number of techniques, superior to Fourier deconvolution, for recovering $\Psi_{\rm obs}(V_z, \tau)$ from relatively poor quality data. These include the maximum entropy method (MEM) of Horne (1994), the regularized linear inversion method of Vio, Horne, & Wamsteker (1994) and Krolik & Done (1995), and the subtractive optimally localized averages (SOLA) method of Pijpers & Wanders (1994).

Our simulations currently utilize the MEM as implemememented in the software package `MEMECHO`, described by Horne (1994). We use `MEMECHO` to fit a linearized echo-mapping model to the data set, defined by the sampled $C(t)$ and $L(V_z, t)$,

$$L(V_z, t) = \bar{L} + \int_0^\infty \Psi_{\rm obs}(V_z, \tau) \left[C(t-\tau) - \bar{C} \right] d\tau, \qquad (2)$$

where $\bar{L}$ and $\bar{C}$ are constant "background" line and continuum fluxes that account for constant contaminating fluxes, such as the host-galaxy starlight contribution to the continuum and narrow emission-line flux to the center of the emission line. The transfer function $\Psi_{\rm obs}(V_z, \tau)$ in the above model represents the marginal responsivity (i.e., relative to some mean level) to changes in the continuum. The linearized echo-mapping model is insensitive to mild non-linear line responsivities and affords an improvement over the simpler linear model of eq. (1). The MEM fit proceeds iteratively, by varying model $C(t)$, $\Psi_{\rm obs}(V_z, \tau)$, and $\bar{L}$ to fit simultaneously the observed $C(t)$ and $L(V_z, t)$. The smoothest positive, i.e., maximum entropy, $\Psi_{\rm obs}(V_z, \tau)$ for which $\chi^2/N \approx 1 \pm \sqrt{2/N}$, with N the number of line and continuum measurements, defines a satisfactory fit to the data. The observed transfer function $\Psi_{\rm obs}(V_z, \tau)$ may be compared with the appropriate model $\Psi_{\rm mod}(V_z, \tau)$ for many artificial data sets.

3. Emission-Line Simulation Results

Here we present some of our preliminary numerical simulations. In §3.1, we compare simulated $\Psi_{\rm obs}(V_z, \tau)$ with associated model $\Psi_{\rm mod}(V_z, \tau)$ to determine the necessary sampling characteristics for an observational monitoring program that will allow us to distinguish among the four different models. In §3.2, we test the verisimilitude of our simulations by simulating the characteristics of a previous observing campaign undertaken with *IUE*; we find that the quality of the transfer functions that we obtain in these simulations is similar to the quality of the transfer functions recovered from the real data.

3.1. Baseline Design for a Monitoring Campaign

We follow the simulation methodology outlined in §2, with sampling and data characteristics appropriate for observations of the C IV emission line in nearby bright Seyfert 1 galaxies (such as NGC 5548 or NGC 7469) made with the original *Kronos* design. Integration times are long enough to achieve $S/N \approx 30$ in each resolution element (~ 1.5 Å). Continuum measurements are binned over 20 Å, leading to $S/N \approx 100$, the design specification for the instrument. For the sake of computational speed, the emission-line response $L(V_z, t)$, is binned into

~ 4 Å bins. We have carried out a large number of simulations, with range of durations $20 \leq T_{\rm dur} \leq 160$ days and time resolutions $0.1 \leq \Delta t \leq 1$ day.

Figures 3–6 present a selection of transfer functions recovered from the simulated data, shown in a format similar to the model transfer functions of Fig. 2. In Figs. 3 and 4, we present mean transfer functions, derived from ~ 10 simulations, i.e., data sets with identical sampling characteristics (S/N, Δt, and $T_{\rm dur}$), and similar but distinct continuum and emission-line variability characteristics. The error bars on $\Psi(\tau)$ and $\Psi(V_z)$ represent the standard deviation σ about the mean transfer function and line profile, and indicate a plausible range of solutions one may expect from any given realization. The mean transfer functions thus have higher signal-to-noise ratios relative to an individual realization, but typically the transfer functions recovered in a single realization are indistinguishable from one another, at least for the longer-duration tests (i.e., $T_{\rm dur} \geq 60$ days; e.g., see Fig. 5). By visual inspection, we find one is able to distinguish clearly among the BLR models shown in Fig. 2 for data sets of duration $T_{\rm dur} \geq 60$ days and resolution $\Delta t \approx 0.1$ day (Fig. 4). For short-duration experiments (Fig. 6) $T_{\rm dur} \ll 60$ days, the recovered transfer functions are ambigious, i.e., they are noisy and permit a range of similarly poor solutions that do not allow us to distinguish among the models. This is consistent with the general rule-of-thumb that a monitoring program should have a duration at least 3 times as long as the maximum time scale to be measured (Penston 1991). The longest-duration experiments ($T_{\rm dur} \gg 60$ days) show little improvement relative to the result for $T_{\rm dur} = 60$ days (Fig. 3). For poorer-resolution experiments, longer data trains are required. Similar, unambigious transfer functions require $T_{\rm dur} = 80$ days for $\Delta t = 0.5$ day and $T_{\rm dur} = 100$ days for $\Delta t = 1.0$ day.

The differences between the model $\Psi_{\rm mod}(V_z, \tau)$ and recovered transfer functions $\Psi_{\rm obs}(V_z, \tau)$, are dominated by uncertainties in the time-dependent response, i.e., in $\Psi_{\rm obs}(\tau)$. To quantify these differences, we calculated the median ratio $\Psi_{\rm mod}(\tau)/\Psi_{\rm obs}(\tau)$, over an appropriate range of time scales, $\tau = 0.5$–16.5 days. The median ratios for the $\Delta t = 0.1$ day experiments were $\sim 30\%$, 25%, 5%, and 25% for Models A, B, C, and D, respectively. The combination of BLR model structural complexity and the employed deconvolution technique affects the accuracy of the recovered transfer functions. The `MEMECHO` maximum-entropy fitting method finds the smoothest, simplest $\Psi_{\rm obs}(V_z, \tau)$ that satisfactorily fits the data. This tends to reduce the structure in the recovered transfer function $\Psi_{\rm obs}(\tau)$ relative to the model $\Psi_{\rm mod}(\tau)$ and gives preference to solutions with Gaussian peaks and exponential tails. Models C and D may be approximated by such structureless functions. Model C is the simplest model by far. In contrast, Model A, is perhaps the most structurally complex model considered. As a result, many of the recovered transfer functions fail to resolve the double-peaked structure in $\Psi(\tau)$ (Fig. 2), thereby adversely affecting the accuracy of our recovered transfer function relative to the other models.

3.2. Comparison with Existing Monitoring Data

In order to assess how accurately these simulations might apply to real data, we have carried out simulations for which the parameters are consistent with an actual observational campaign that has been previously undertaken. We consider specifically the 1996 *IUE* campaign on NGC 7469 (Wanders et al. 1997),

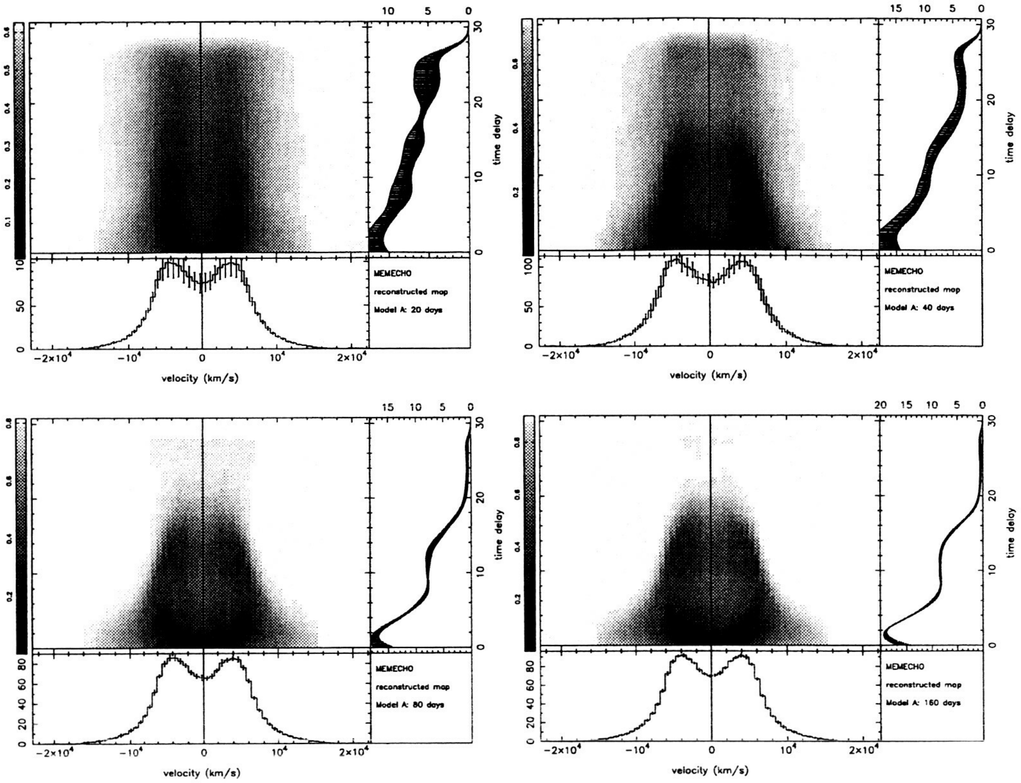

Figure 3. Mean observed transfer functions $\langle\Psi(V_z,\tau)_{\rm obs}\rangle$ for Model A, §2.2. The artificial data sets are characterized by continuum and emission-line flux uncertainties of 1 and 3%, respectively, temporal resolution Δt = 0.1 day, monitoring duration $T_{\rm dur}$ = 20 days (upper left), $T_{\rm dur}$ = 40 days (upper right), $T_{\rm dur}$ = 80 days (lower left), and $T_{\rm dur}$ = 160 days (lower right). The format is similar to Fig. 2. The error bars on $\Psi(\tau)$ and $\Psi(V_z)$ are the standard deviation σ about the mean transfer function and variable line profile, and indicate a plausible range of solutions one may expect from any given data set. For $T_{\rm dur} \geq 60$ days, we reliably define the transfer function as that of Model A. See §3.1 for further discussion.

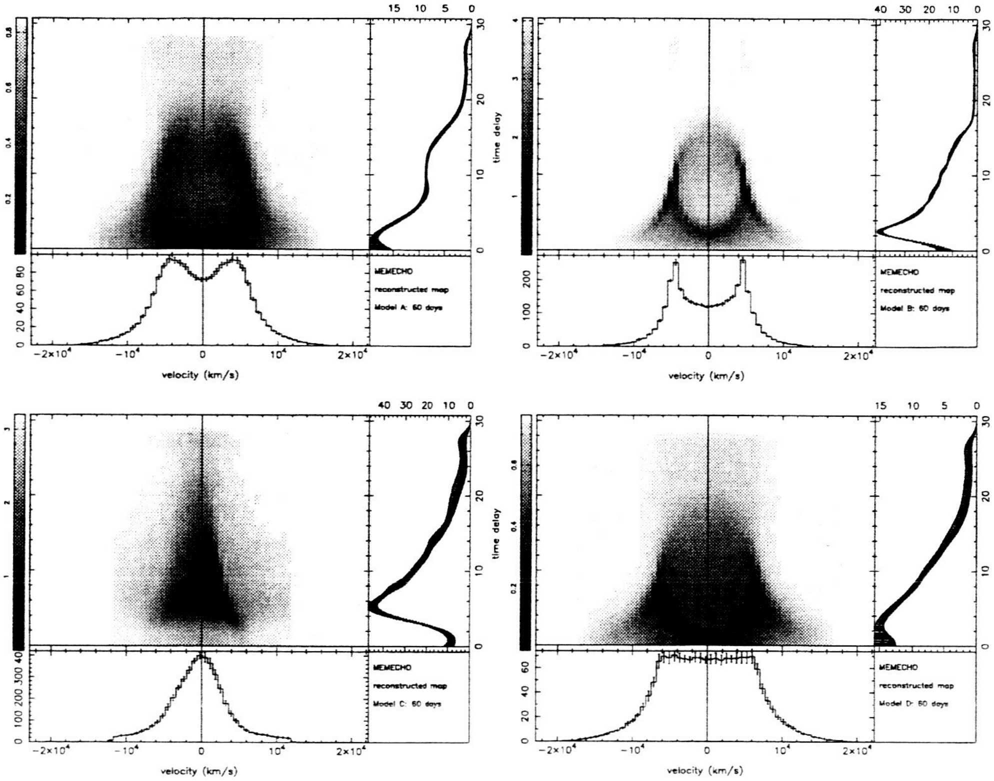

Figure 4. Mean observed transfer functions $\langle \Psi(V_z, \tau)_{\rm obs} \rangle$ for Models A–D, as labelled. The artificial data sets are characterized by continuum and emission-line flux uncertainties of 1 and 3%, respectively, monitoring durations, $T_{\rm dur} = 60$ days, and temporal resolutions $\Delta t = 0.1$ day. This figure should be compared directly with the model transfer functions shown in Fig. 2. We may clearly distinguish among the four BLR models for data sets with $T_{\rm dur} = 60$ days and $\Delta t = 0.1$ day. Similar, unambigious transfer functions require $T_{\rm dur} \approx 80$ and 100 days for $\Delta t = 0.5$ and 1 day, respectively. See §3.1 for additional discussion.

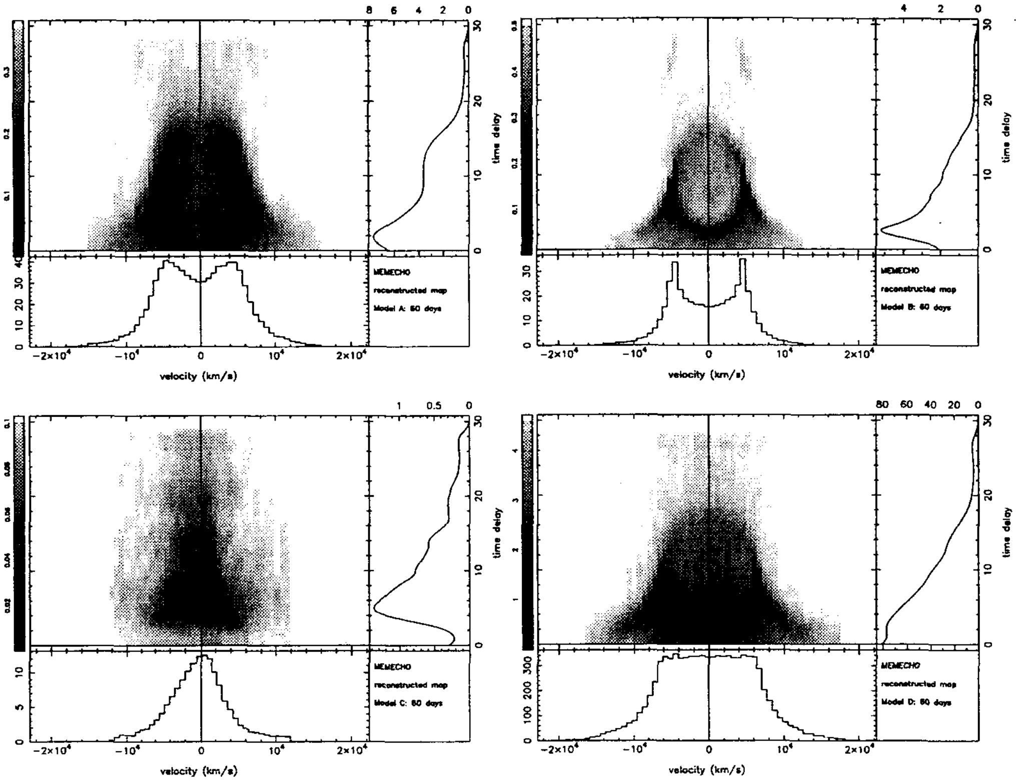

Figure 5. Observed transfer functions $\Psi(V_z, \tau)_{\rm obs}$ for Models A–D (§2.2) and monitoring duration $T_{\rm dur} = 60$ days, as labelled. The artificial data sets are characterized by continuum and emission-line flux uncertainties of 1 and 3%, respectively, and temporal resolutions $\Delta t = 0.1$ day. The format is the same as Fig. 2. The recovered $\Psi(V_z, \tau)_{\rm obs}$ permit a reliable distinction among the four BLR models, from which accurate model parameters may be inferred. The individual $\Psi(V_z, \tau)_{\rm obs}$ may be contrasted with the appropriate mean $\langle\Psi(V_z, \tau)_{\rm obs}\rangle$ of Fig. 4 and the corresponding model transfer functions in Fig. 2. For these data sets, the results of individual realizations are essentially indistinguishable. See §3.1 for further discussion.

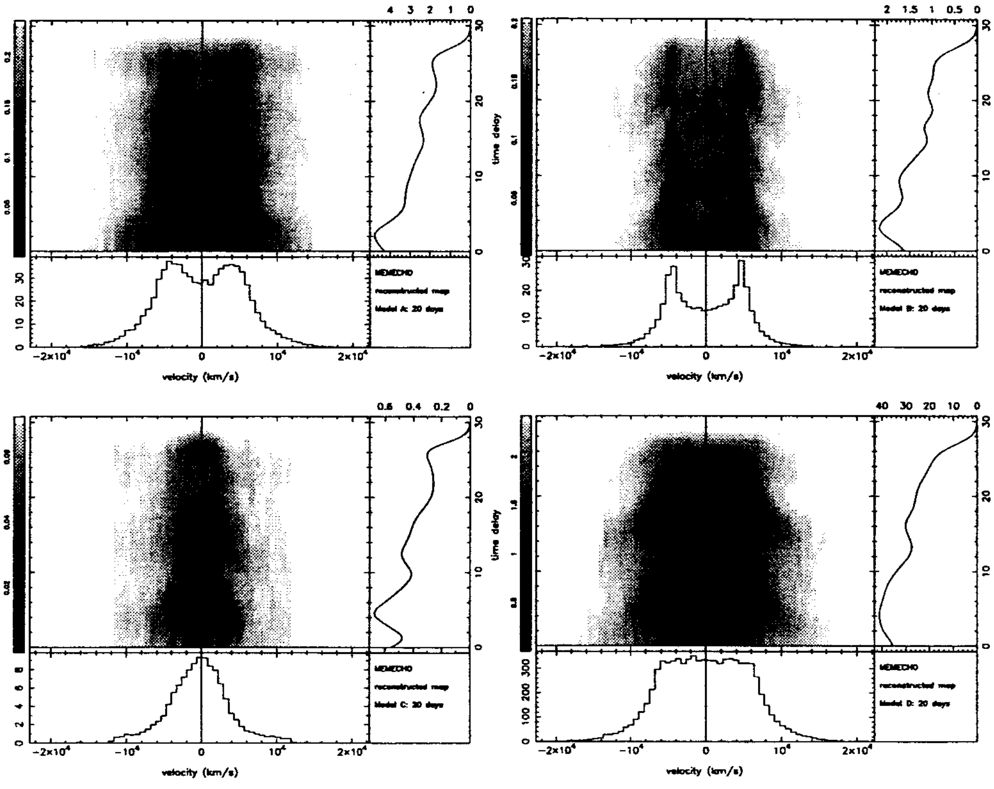

Figure 6. Observed transfer functions $\Psi(V_z, \tau)_{\rm obs}$ for Models A–D (§2.2) and monitoring duration $T_{\rm dur} = 20$ days, as labelled. The artificial data sets are characterized by continuum and emission-line flux uncertainties of 1 and 3%, respectively, and temporal resolutions $\Delta t = 0.1$ day. The format is the same as Fig. 2. The recovered $\Psi(V_z, \tau)_{\rm obs}$ are noisy and permit a range of similarly poor solutions. They do not permit a reliable distinction among all four BLR models nor accurate characterization of any individual model. These may be compared directly with the recovered transfer functions based on 60-day experiments, shown in Fig. 5. See §3.1 for additional discussion.

which arguably represents the current state of the art. We adopt simulation parameters: (a) $T_{\rm dur} = 49$ days, (b) $\Delta t = 0.2$ days, (c) continuum and emission-line flux uncertainties of 3% and 7%, respectively, (d) spectral resolution ~ 8 Å, and (e) $F_{\rm var} = 0.12$ on time scales of 10 days. These *IUE*-type simulations may be contrasted with similar, albeit at different spectral resolution, *Kronos* simulations with continuum and emission-line flux uncertainties of 1% and 3%, respectively.

Figure 7 presents the recovered transfer functions for Models A and B for *IUE*-quality data and for *Kronos*-type data. It is clear that the *IUE*-type simulations do not have sufficient S/N and/or duration to distinguish between these two competing BLR models. However, the improved continuum and emission-line signal-to-noise ratios afforded by *Kronos* would enable us to distinguish between these two cases with at least limited success. It is also instructive to compare the *Kronos*-type simulations in Fig. 7 with those in Fig. 4, which are based on an experiment with a duration only 20% longer.

4. Interband Continuum Simulation Methodology

The aim of our interband continuum simulations is definition of the observational criteria for successful detection of wavelength-dependent time delays. For the sake of specificity; we consider a simple "lamp post" reprocessing model, where an X-ray source on the axis of a thin accretion disk illuminates the disk from above. The X-ray variations are assumed to induce local temperature variations in the disk, which results in variable UV/optical fluxes. This is a simple, heuristic model, but it has the virtue that the variability signal is transmitted radiatively, so the time scales involved are fast: any slower mechanism would be even easier to detect through multiwavelength monitoring.

For each synthetic data set, we generate artificial short-wavelength (say, X-ray) light curves $S_{\rm X}$ of length $T_{\rm dur}$ from a plausible power-density spectrum distribution, as described in §2.1. We normalize $S_{\rm X}$ to have fractional flux variations $F_{\rm var} = 0.15$ over 21 days, as was observed for NGC 7469 by Nandra et al. (1998). We convolve $S_{\rm X}(t)$ with the time-dependent response of the disk to X-ray illumination, i.e., a transfer function $\Psi(\lambda, \tau, t)$, to predict associated reprocessed UV/optical variations $F_\lambda(t)$. Explicitly,

$$F_\lambda(t) = \int \Psi(\lambda, \tau, t) S_{\rm X}(t - \tau) d\tau. \tag{3}$$

The instantaneous transfer function $\Psi(\lambda, \tau)$ is defined by

$$\Psi(\lambda, \tau) = \int_{R_{\rm min}}^{R_{\rm max}} B_\nu \left(T(R)\right) 2\pi R \, dR, \tag{4}$$

with B_ν the Planck function, $R_{\rm min}$ and $R_{\rm max}$ the inner and outer disk radii, respectively, and $T(R)$ the accretion-disk temperature profile. We assume the temperature profile is a non-linear combination of surface temperature due to a combination of (a) viscous heat dissipation via gravitational torques and (b) irradiation effects, thereby depending on the accretion-disk geometry and relative

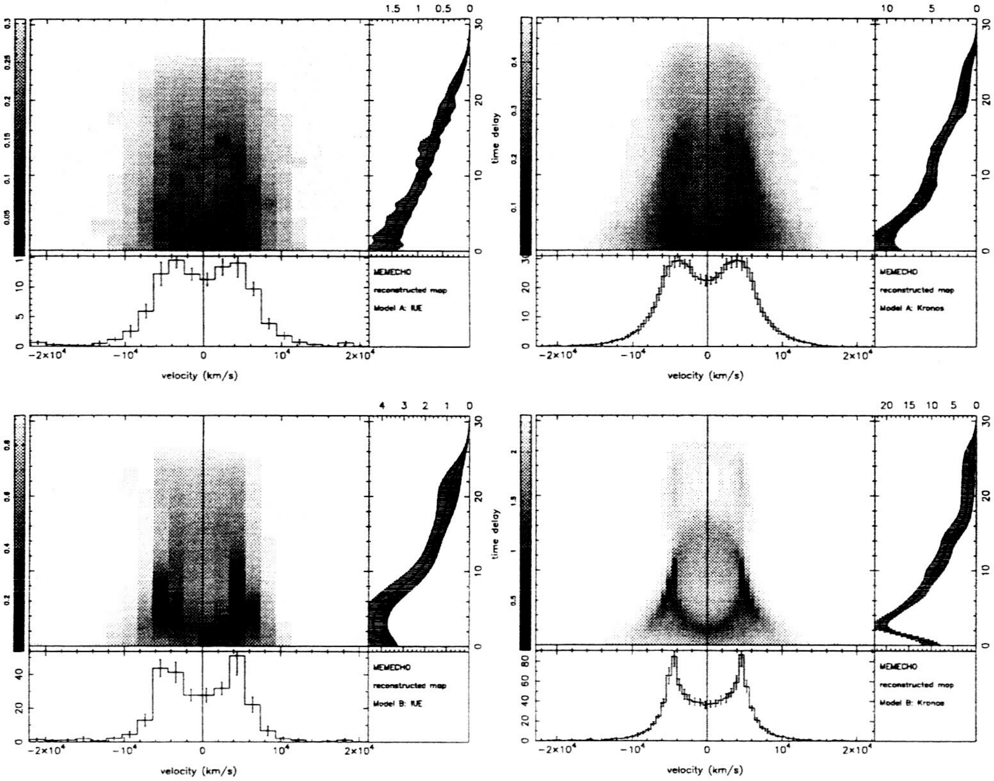

Figure 7. Comparison of mean observed transfer functions $\langle\Psi(V_z,\tau)_{\rm obs}\rangle$ for Models A and B (§2.2), derived from *IUE*-like and *Kronos*-like data sets; the left-hand panels are *IUE*-like data sets (top: Model A; bottom: Model B), and the right-hand panels show the corresponding *Kronos*-like data sets. The *IUE*-like artifical data sets mimic the characteristics of a 49-day, 0.2-day resolution UV monitoring campaign on NGC 7469, as described by Wanders et al. (1997). It is clear that existing archival data sets do not have sufficient S/N and/or duration to reliably distinguish between these two competing BLR models. See §3.2 for a more complete discussion.

prominence of viscous heat dissipation and irradiation effects, i.e.,

$$T^4 = \frac{3GM\dot{M}}{8\pi\sigma R^3} + \left(\frac{(1-A)L_X}{4\pi\sigma(R^2+H_X^2)^2}\right)\cos\theta_X, \tag{5}$$

where M, $\dot{M}$, A, and $\cos\theta_X$ are the black-hole mass, accretion rate, X-ray disk albedo, and angle between the disk normal and X-ray illuminating source, respectively. The disk is illuminated by a point source of luminosity L_X at a height H_X above the disk midplane (Rokaki & Magnan 1992; Berkley et al. 2000). We note Berkley et al. (2000) do not include the contribution of viscous heat dissipation to $T(R)$, and this probably partly explains the large discrepancies between their model and observed UV/optical lags for NGC 7469. The radial temperature profile is $T \propto R^{-3/4}$ for $R \gg H_X$. We adopt nominal, plausible disk parameters; $M = 10^7\,M_\odot$, $\dot{M} = 0.07\,M_\odot\,\mathrm{yr}^{-1}$, $A = 0.5$, $H_X = 0.05$ light day, and $L_X = 10^{44}$ ergs s^{-1}. We expect delays of order days between variations at 1300 Å and 9000 Å for nearby, bright Seyfert 1 galaxies (Peterson et al. 1998).

The reprocessed light curves are re-normalized to have fractional flux variations consistent with observations, and appropriate Gaussian distributed noise is added. Finally, the light curves are cross-correlated with the interpolated cross-correlation algorithm described by White & Peterson (1994) to determine peak and centroid time lags. The whole process is repeated ~ 100 times to build up peak and centroid cross-correlation distributions from which meaningful statistics, such as the median centroid and peak lags, may be calculated.

5. Interband Continuum Simulation Results

We consider two specific types of experiments that might be undertaken in an attempt to detect interband continuum lags:

1. *Optical ground-based observations.* We consider whether interband continuum variations might be detectable using optical ground-based observations alone. We consider experiments utilizing a single telescope (time resolution $\Delta t = 1$ day) or two telescopes widely spaced in longitude ($\Delta t = 0.5$ day).
2. *UV/optical space-based observations.* We consider the advantages of carrying out similar experiments in space, where UV spectral coverage and high time resolution are attainable.

5.1. Simulations of Ground-Based Monitoring

We suppose observations are made at wavelengths representative of $BVRI$ filters, i.e., 4400, 5500, 7000, and 9000 Å. We renormalize the multicolor variations to $F_{\mathrm{var}} = 0.04$, 0.04, 0.02, and 0.02 for B, V, R, and I, respectively, on time scales of 10 days (see Fig. 1), and add Gaussian distributed noise of amplitude 1%. Sets of optical lightcurves for monitoring durations of 4, 6, 8, and 10 weeks, with 1-day resolution (simulating a single telescope) and 0.5-day resolution (simulating a pair of telescopes) were generated. To simulate the effects of bad weather we randomly reject 25% of the points from each light curve. For the accretion-disk model described in §4, time lags relative to B are 0.13, 0.32, and 0.59 days for the V, R, and I light curves.

Our results for 1-day and 0.5-day resolution are shown in Tables 1 and 2, respectively. For both, the first column gives the monitoring duration, and the following columns give for the color pairs B/V, B/R, and B/I the value of the median cross-correlation centroid distribution (with 68.3% confidence limits[1]) and the probability that a single simulation will yield a value $\tau_{\text{cen}} \leq 0$ (which is thus a confidence limit for detection of a positive, non-zero lag).

Table 1. Simulations for Optical Ground-Based Monitoring with $\Delta t = 1.0$ day

T_{dur} (weeks)	$\tau_{\text{cen}}(BV)$ (days)	$P \leq 0$	$\tau_{\text{cen}}(BR)$ (days)	$P \leq 0$	$\tau_{\text{cen}}(BI)$ (days)	$P \leq 0$
4	$0.11^{+0.15}_{-0.10}$	0.13	$0.25^{+0.24}_{-0.24}$	0.09	$0.44^{+0.17}_{-0.34}$	0.07
6	$0.11^{+0.14}_{-0.10}$	0.12	$0.24^{+0.18}_{-0.25}$	0.07	$0.46^{+0.24}_{-0.21}$	0.03
8	$0.11^{+0.13}_{-0.11}$	0.15	$0.24^{+0.20}_{-0.23}$	0.12	$0.49^{+0.15}_{-0.20}$	0.03
10	$0.11^{+0.15}_{-0.10}$	0.16	$0.25^{+0.19}_{-0.15}$	0.04	$0.48^{+0.21}_{-0.17}$	0.03

Table 2. Simulations for Optical Ground-Based Monitoring with $\Delta t = 0.5$ day

T_{dur} (weeks)	$\tau_{\text{cen}}(BV)$ (days)	$P \leq 0$	$\tau_{\text{cen}}(BR)$ (days)	$P \leq 0$	$\tau_{\text{cen}}(BI)$ (days)	$P \leq 0$
4	$0.10^{+0.10}_{-0.10}$	0.14	$0.20^{+0.20}_{-0.13}$	0.10	$0.35^{+0.20}_{-0.20}$	0.05
6	$0.10^{+0.09}_{-0.09}$	0.07	$0.20^{+0.19}_{-0.10}$	0.05	$0.40^{+0.20}_{-0.15}$	0.01
8	$0.10^{+0.09}_{-0.09}$	0.09	$0.24^{+0.18}_{-0.13}$	0.06	$0.44^{+0.16}_{-0.18}$	0.01
10	$0.10^{+0.09}_{-0.05}$	0.06	$0.24^{+0.11}_{-0.10}$	0.01	$0.40^{+0.23}_{-0.11}$	0.03

For 1-day resolution experiments and $T_{\text{dur}} = 4$–10 weeks, we are not able to resolve delays $\lesssim 0.3$ day with notable confidence. We begin to resolve non-zero delays, for example between B and I, of ~ 0.5 days for $T_{\text{dur}} \geq 6$ weeks with about 97% confidence. For larger relative delays (say ~ 1.5 days), predicted in the case of larger black-hole mass systems, we may expect to measure delays with $\gtrsim 99\%$ confidence. Note we may resolve delays that are about a factor of 2 smaller than our temporal sampling. We are effectively able to resolve delays somewhat smaller than our Nyquist limit due to the smooth, featureless character of UV/optical variations on time scales $\lesssim 0.5$ days. The rapidly falling power-density spectrum has been confirmed by continuous monitoring of NGC 7469 by Welsh et al. (1998). The lack of power on these short time scales permits us to use linear interpolation in our cross-correlation analysis and recover significant differences at delays of $\lesssim 0.5$ days.

---

[1] These would correspond to 1-σ limits for a normal distribution. However, the cross-correlation delay distributions are typically non-normal (e.g., Maoz & Netzer 1989), rendering the standard deviation of the distribution a poor characterization of the lag uncertainty.

Our ability to accurately resolve optical delays is enhanced by increasing our monitoring resolution, i.e., utilizing co-ordinated observations at multiple observatories. For 0.5-day resolution experiments and $T_{\rm dur} \geq 6$ weeks, we are able to resolve delays as short as ~ 0.5 day with $\gtrsim 99\%$ confidence, noting the decrease in detection efficiency for the 10-week campaign is most likely a statistical fluke.

Our reasoning for adopting the centroid, rather than the location of the peak value, of the cross-correlation function deserves attention in light of a recent discussion by Welsh (1999). Welsh (1999) showed that peak and centroid lags are biased towards values that are too low because of finite-duration sampling and long time-scale trends in light curves. The peak was found to be a less biased and more accurate measure of the expected lag for a simple Gaussian transfer function model. We find both the centroid and peak lag measurements are too low relative to their expected values, with biases sometimes as large as $\sim 30\%$. However, we find the majority of our centroid lag biases are a consequence of how we define the centroid measurement. Typically, the centroid lag is calculated over all points above some threshold, defined by $0.8\, r_{\rm max}$ with $r_{\rm max}$ the maximum cross-correlation amplitude. We note, by eliminating the threshold (i.e., including all points near the cross-correlation peak with $r > 0$), we reduce our biases significantly, to $\leq 10\%$, with the remainder possibly attributable to finite-duration sampling and long time-scale trends. The operational definition of the centroid lag needs to be revisited. Typically, the centroid lags show larger variance than the peak lags, but the centroid measurements are less-biased estimators of the expected lag, defined by the centroid of the model transfer function (see also Pérez et al. 1992). This is a consequence of our more complex, extended transfer function model, and demonstrates that the conclusions of Welsh (1999) may not be applicable to more complex transfer-function models, e.g., disk and thick spherical geometries. Hence, we adopt the median centroid lag rather than the peak, since while displaying a larger variance, its 1σ confidence range typically includes the predicted lag.

5.2. Simulations of Space-Based Monitoring

The disk model described in §4 yields a predicted interband continuum delay of ~ 0.04 day between variations at 1300 Å and 1800 Å, difficult to resolve without a dedicated monitoring platform, such as *Kronos*. We consider here whether or not interband continuum lags could be detected from a satellite in low-Earth orbit, such as *HST*. We consider a somewhat higher-luminosity source (such as NGC 5548) than in the previous section, using model parameters $M = 10^8\, M_\odot$, $\dot{M} = 0.7\, M_\odot\, {\rm yr}^{-1}$, $A = 0.5$, $H_{\rm X} = 0.05$ light day, and $L_{\rm X} = 10^{44}$ ergs s^{-1}.

We choose nominal line-free wavelengths of 1300 Å, 1480 Å, 1800 Å, and renormalize the light curves to $F_{\rm var} = 0.05$ on time scales of 10 days, which is a conservative estimate. As before, we add Gaussian distributed noise with amplitude 1%, and generate sets of UV light curves for $T_{\rm dur} = 1$, 2, and 3 weeks, with time resolution 0.2 and 0.1 day resolution. To simulate the effects of bad or lost data, we randomly reject 5% of the data from each light curve. The model time lags, relative to 1300 Å, are 0.05 and 0.14 days for 1480 Å and 1800 Å.

Full results for our 0.2 and 0.1 day resolution simulations are listed in Tables 3 and 4, respectively, in the same format used in Tables 1 and 2. For 0.2-

day resolution experiments, we expect to resolve non-zero delays of about 0.1 day for $T_{\rm dur} \approx 2$ weeks with $\gtrsim 99\%$ confidence. Furthermore, we may resolve longer UV/optical delays at similar confidence levels. This type of experiment is realizable with ~ 70 *HST* orbits.

Table 3. Simulations for UV Space-Based Monitoring with $\Delta t = 0.2$ day

$T_{\rm dur}$ (weeks)	$\tau_{\rm cen}$ (1300–1480 Å) (days)	$P \leq 0$	$\tau_{\rm cen}$ (1300–1800 Å) (days)	$P \leq 0$
1	$0.03^{+0.03}_{-0.03}$	0.10	$0.08^{+0.04}_{-0.04}$	0.03
2	$0.03^{+0.04}_{-0.02}$	0.08	$0.09^{+0.03}_{-0.03}$	0.00
3	$0.03^{+0.03}_{-0.02}$	0.00	$0.10^{+0.05}_{-0.03}$	0.00

Table 4. Simulations for UV Space-Based Monitoring with $\Delta t = 0.1$ day

$T_{\rm dur}$ (weeks)	$\tau_{\rm cen}$ (1300–1480 Å) (days)	$P \leq 0$	$\tau_{\rm cen}$ (1300–1800 Å) (days)	$P \leq 0$
1	$0.03^{+0.03}_{-0.02}$	0.06	$0.08^{+0.03}_{-0.03}$	0.01
2	$0.03^{+0.03}_{-0.02}$	0.04	$0.09^{+0.05}_{-0.03}$	0.00
3	$0.03^{+0.02}_{-0.02}$	0.02	$0.10^{+0.04}_{-0.04}$	0.00

6. Summary

Echo-mapping techniques may be used to strongly constrain the nature of AGN central engines on milliparsec scales. These techniques allow us (a) to determine the geometry and kinematics of the broad-line emission regions, thereby permitting accurate black-hole mass measurements, and (b) to measure radial temperature profiles of continiuum emission regions and determine the physical mechanisms responsible. These simulations demonstrate successful echo-mapping programs are resource-intensive, and will require a dedicated multi-wavelength space-based monitoring platform.

Some of the specific conclusions we have reached in these preliminary echo-mapping numerical simulations are;

1. Even the best existing monitoring data sets do not have sufficient signal-to-noise ratios and monitoring duration to place strong constraints on the BLR gas distribution; the observations may be accomodated by a number of plausible BLR models.

2. An UV monitoring campaign of duration $T_{\rm dur} \approx 60$ days, time resolution $\Delta t \approx 0.1$ day, and continuum and emission-line flux uncertainties of $\sim 1\%$ and $\sim 3\%$, respectively, will strongly constrain the geometry and kinematics of the BLR, and thereby permit accurate black-hole mass measurements.

3. We may expect to detect interband continuum delays of $\gtrsim 0.5$ days (in nearby AGNs) with $\gtrsim 97\%$ confidence for optical ground-based monitoring of duration $T_{\rm dur} \approx 42$ days, time resolution $\Delta t \approx 1$ day with flux measurements that are accurate to $\sim 1\%$. Delays of similar magnitude may be detected with $\gtrsim 99\%$ confidence with a space-based monitoring campaign of $T_{\rm dur} \approx 14$ days and $\Delta t \approx 0.2$ day.

Acknowledgments. The authors are grateful to NASA for support of these simulations through grant NAG5-8397 to The Ohio State University.

References

Bahcall, J.N., Kozlovsky, B.-Z., & Salpeter, E.E. 1972, ApJ, 171, 467
Berkley, A., Kazanas, D., & Ozik, J. 2000, ApJ, 535, 712
Blandford, R., & McKee, C. 1982, ApJ, 255, 419
Capriotti, E.R., Foltz, C.B., & Peterson, B.M. 1982, ApJ, 261, 35
Chiang, J., Reynolds, C.S., Blaes, O.M., Nowak, M.A., Murray, N., Madejski, G., Marshall, H.L., & Magdziarz, P. 2000, ApJ, 528, 292
Clavel, J., et al. 1991, ApJ, 366, 64
Clavel, J., et al. 1992, ApJ, 393, 113
Collier, S., et al. 1998, ApJ, 500, 162
Collier, S., Horne, K., Wanders, I., & Peterson, B. M. 1999, MNRAS, 302, L24
Crenshaw, D.M., & Blackwell, J.H., Jr. 1990, ApJL, 358, L37
Done, C., & Krolik, J. 1996, ApJ, 463, 144
Edelson, R., et al. 1996, ApJ, 470, 364
Edelson, R., et al. 2000, ApJ, 534, 180
Emmering, R., Blandford, R., & Shlosman, I. 1992, ApJ, 385, 460
Fabrika, S.N. 1980, Soviet Astr. Lett., 6, 293
Goad, M., & Wanders, I. 1996, ApJ, 469, 113
Green, P., McHardy, I., & Lehto, H. 1993, MNRAS, 265, 664
Horne, K. 1994, in Reverberation Mapping of the Broad-Line Region in Active Galactic Nuclei, ed. P.M. Gondhalekar, K. Horne, & B.M. Peterson (San Francisco: ASP), p. 23
Horne, K. 1999, in Quasars and Cosmology, ed. G. Ferland & J. Baldwin (San Francisco: ASP), p. 189
Korista, K.T., et al. 1995, ApJS, 97, 285
Kriss, G.A., Peterson, B.M., Crenshaw, D.M., & Zheng, W. 2000, ApJ, 535, 58
Krolik, J., & Done, C. 1995, ApJ, 440, 166
Lawrence, A., & Papadakis, I. 1993, ApJ, 414, 85
Maoz, D., & Netzer, H. 1989, MNRAS, 236, 21
Marshall, H., et al. 1997, ApJ, 479, 222
Nandra, K., et al. 1998, ApJ, 505, 594
Nandra, K., et al. 2000, ApJ, in press

Netzer, H., & Peterson, B. M. 1997, in Astronomical Time Series, ed. D. Maoz, A. Sternberg, & E.M. Leibowitz (Dordrecht: Kluwer Academic Publishers), p. 85

Penston, M.V. 1991, in Variability of Active Galactic Nuclei, ed. H.R. Miller, & P.J. Wiita (Cambridge: Cambridge University Press), p. 343

Pérez, E., Robinson, A., & de La Fuente, L. 1992, MNRAS, 255, 502

Peterson, B.M. 1993, PASP, 105, 247

Peterson, B.M., & Wandel, A. 2000, ApJ, 540, L13

Peterson, B.M., et al. 1991, ApJ, 368, 119

Peterson, B.M., et al. 1998, PASP, 110, 660

Pijpers, F., & Wanders, I. 1994, MNRAS, 271, 183

Rokaki, E., & Magnan, C. 1992, A&A, 261, 41

Ulrich, M.-H., & Horne, K. 1996, MNRAS, 283, 748

Vio, R., Horne, K., & Wamsteker, W. 1994, PASP, 106, 1091

Wanders, I., et al. 1995, ApJ, 453L, 87

Wanders, I., et al. 1997, ApJS, 113, 69

Welsh, W.F. 1999, PASP, 111, 1347

Welsh, W.F., & Horne, K. 1991, ApJ, 379, 586

Welsh, W.F., Peterson, B.M., Koratkar, A.P., & Korista, K.T. 1998, ApJ, 509, 118

White, R.J., & Peterson, B.M. 1994, PASP, 106, 879